Available online at www.sciencedirect.com
ScienceDirect
Respiratory Physiology & Neurobiology 161 (2008) 125–135
RESPIRATORY PHYSIOLOGY & NEUROBIOLOGY
www.elsevier.com/locate/resphysiol

Numerical simulations for detailed airflow dynamics in a human nasal cavity

Jian Wen, Kiao Inthavong, Jiyuan Tu *, Simin Wang

School of Aerospace, Mechanical and Manufacturing Engineering, RMIT University, PO Box 71, Plenty Road, Bundoora, Victoria 3083, Australia

Accepted 17 January 2008

Abstract

Nasal physiology is dependent on the physical structure of the nose. Individual aspects of the nasal cavity such as the geometry and flow rate collectively affect nasal function such as the filtration of foreign particles by bringing inspired air into contact with mucous-coated walls, humidifying and warming the air before it enters the lungs and the sense of smell. To better understand the physiology of the nose, this study makes use of CFD methods and post-processing techniques to present flow patterns between the left and right nasal cavities and compared the results with experimental and numerical data that are available in literature. The CFD simulation adopted a laminar steady flow for flow rates of 7.5 L/min and 15 L/min. General agreement of gross flow features were found that included high velocities in the constrictive nasal valve area region, high flow close to the septum walls, and vortex formations posterior to the nasal valve and olfactory regions. The differences in the left and right cavities were explored and the effects it had on the flow field were discussed especially in the nasal valve and middle turbinate regions. Geometrical differences were also compared with available models.

Keywords: Nasal cavity; Modelling; Airflow; CFD; Nose; Simulation

1. Introduction

The human nasal cavity is an important component to the respiratory system, which performs a variety of physiological functions. It is responsible for heating and humidifying inspired air to near body core temperature with full saturation, while filtering the air from pollutants and toxic particles that may enter the airway. On the other hand, the nasal cavity provides an alternative route for drug delivery. Deposition sites on the highly vascularised mucosal walls provide improved speed of pharmacological action and retention of the drug composition, which is often destroyed when drugs are digested. Detailed airflow patterns can provide data that is pertinent to the prediction of gas–particle flows and regional tissue exposure to inhaled air. The numerical data which can produce highly quantitative results ideally complements existing experimental data that often lack fine details.

The nasal anatomy, characterized by thin airway channels does not allow direct measurements of flow patterns inside the human nose. Instead rigid cast models have been used to experimentally study the airflow patterns by a number of researchers. Kelly et al. (2000) investigated two-dimensional velocity fields in parallel planes to the flow direction, throughout a nasal cavity model using particle image velocimetry (PIV). Hahn et al. (1993) used a hot-film anemometer probe to measure the velocity distributions on five cross-sections of a 20× enlarged human nasal cavity model. In these experiments a steady non-oscillatory flow was applied and the flow was considered laminar up to a flow rate of 24 L/min. It was reported that approximately half of the inspired airflow passed through the middle and inferior airways while a small fraction of the flow passed through olfactory slit. Churchill et al. (2004) studied airflow patterns using water and dye flowing through anatomically accurate acrylic models of 10 different human nasal cavities. It was found that the nasal morphological features such as the inferior orientation of the nostrils, the relative size of the nasal valve and the height of the nasal sill did not show statistically significant correlations among the 10 models. However, one parameter, the projection of the turbinate bones into the nasal cavity was shown to laminate the flow.

* Corresponding author. Tel.: +61 3 9925 6191; fax: +61 3 9925 6108.
E-mail address: Jiyuan.Tu@rmit.edu.au (J. Tu).

1569-9048/$ – see front matter © 2008 Elsevier B.V. All rights reserved.
doi:10.1016/j.resp.2008.01.012

Recent developments in medical imaging (MRI and CT scanning) coupled with computational science have opened new possibilities for physically realistic numerical simulations of nasal airflow. Keyhani et al. (1995) examined airflow through one side of the human nose in a three-dimensional model that was truncated anterior to the nasopharynx. Subramaniam et al. (1998) simulated the airflow structures of rest and light breathing conditions (15 L/min and 26 L/min) using a laminar flow. In these studies, flows through both nostrils were performed, however, the airflow patterns on both sides were not compared. Other airflow studies include the work by Zamankhan et al. (2006) and Wang et al. (2005) which briefly discussed airflows through one nasal cavity only.

Intersubject variations in nasal anatomy will cause variations in nasal flow patterns, which is a concern when trying to use the results of a single model. Therefore, this CFD study presents flow patterns between the left and right nasal cavities and compares the results with experimental and numerical data that are available in literature. The CFD simulation adopted a laminar steady flow for flow rates of 7.5 L/min and 15 L/min. CFD methods are advantageous in its ability to provide detailed data that are normally difficult to produce through experiments due to intervention and clinical risks for the volunteer. General agreement of gross flow features that are likely to remain unchanged between subjects are discussed. Additionally the variations in flow patterns and flow features such as pressure drop, wall shear stress, velocity and flow distribution between the left and right cavity as well as different geometries are also presented. The flow in the nasal valve and turbinate region was also studied in particular detail, since the airflow profiles in these regions have not been well investigated.

1.1. Nasal physiology and flow rates

In the following descriptions, the $+X$ coordinate axis is from the anterior tip of the nostril inlet to the nasopharynx which is referred to as the axial direction. The nose can be divided axially into four regions: the vestibule, the nasal valve, the turbinate and the nasopharynx regions. The first three-quarters of the nasal cavity is divided into the left and right cavity separated by the nasal septum wall. Air enters each cavity through the oval shaped external nostrils into the vestibule. The flow changes direction, 90° towards the horizontal, before entering the nasal valve region. The flow increases in this region where the cross-sectional area is smallest causing an acceleration of the air. At the end of the nasal valve region the cross-sectional area of the nasal cavity increases suddenly. This expansion is the beginning of the turbinate region where the profile is complicated and asymmetrical. Finally, at the nasopharyngeal region, the left and right cavities merge together causing the flow in this region to mix intensely.

The main factors that contribute to the airflow patterns are the nasal cavity geometry and the flow rate. For a realistic human nasal cavity, the left and right sides of the nasal cavity differ geometrically while nasal morphological differences can be found between individuals. The inspiratory flow rates for adults can range between 5 L/min and 12 L/min for light breathing and 12–40 L/min for non-normal conditions such as during exertion and physical exercise. Usually breathing switches from pure nasal flow to oral-nasal flow at this higher range. Additionally flow rates for extreme forced inhalation conditions have been found to reach 150 L/min (Robert, 2001).

2. Methods

2.1. Grid generation and grid independence

The nasal cavity geometry was obtained through a CT scan of the nose of a healthy 25-year old, Asian male (170 cm height, 75 kg mass) (as shown in Fig. 1). The CT scan was performed using a CTI Whole Body Scanner (General Electric). The single-matrix scanner was used in helical mode with 1-mm collimation, a 40-cm field of view, 120 kV peak and 200 mA. The scans captured outlined slices in the X–Y plane at different positions along the Z-axis from the entrance of the nasal cavity to just anterior of the larynx at intervals of 1–5 mm depending on the complexity of the anatomy. The coronal-sectioned scans were imported into a three-dimensional (3D) modelling program called GAMBIT (ANSYS Inc., USA) which created smooth curves that connected points on the coronal sections. Stitched surfaces were then created to form a complete computational mesh. Because the details of the flow velocity and pressure were not known prior to the solution of the flow problem, the outlet boundary condition was defined as an outflow with zero diffusion flux for all flow variables in the direction normal to the exit plane. This implies that the flow characteristics have to be consistent with a fully developed flow assumption and a straight extension of the outlet plane was created into the geometry to satisfy this criterion.

An initial model with 82,000 unstructured tetrahedral cells was initially used to solve the airflow field at a flow rate of 15 L/min. The model was then improved by cell adaptation

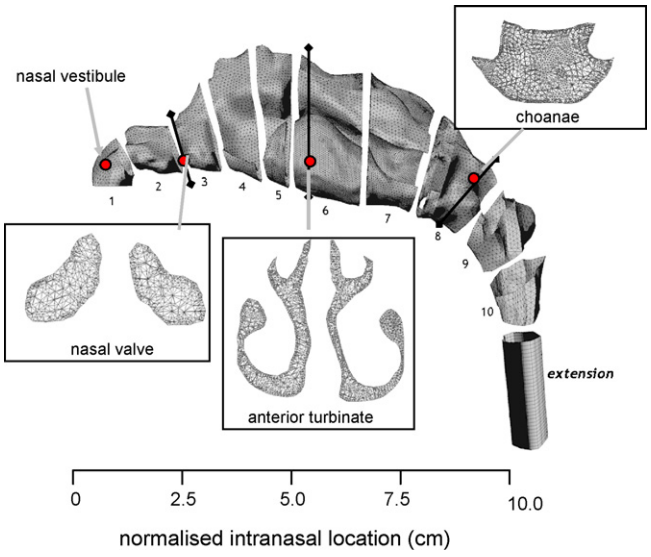

Fig. 1. Nasal cavity model used in the study. Cross-sectional areas taken at the nasal valve, middle turbinate and nasopharynx regions are shown with the computational mesh.

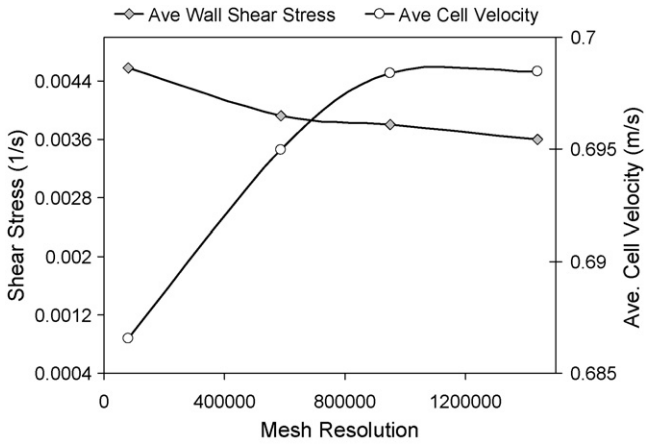

Fig. 2. Shear stress and velocity profiles of a coronal section near the nasal valve region for the four different cavity models.

techniques that included refining large volume cells, cells that displayed high velocity gradients and near wall refinements, where a model with a higher cell count was produced. This process was repeated twice, with each repeat producing a model with a higher cell count than the previous model. Subsequently four models were produced, 82,000, 586,000, 950,000 and 1.44 million cells. A grid independence test shown in Fig. 2, found the results for average velocity and the wall shear stress converge as the mesh resolution approached 950,000 cells. In order to make a compromise between the result's accuracy and computational cost, a model with 950,000 elements was used in this study.

2.2. Fluid flow modelling

Due to the complex geometry of the nasal cavity a commercial CFD code, FLUENT, was utilised to predict the continuum gas phase flow under steady-state conditions through solutions of the conservation equations of mass and momentum. These equations were discretised using the finite volume approach. The third-order accurate QUICK scheme was used to approximate the momentum equation while the pressure–velocity coupling was resolved through the SIMPLE method. Flow rates of 7.5 L/min and 15 L/min were used to simulate light adult breathing. At this flow rate, the flow regime has been determined to be laminar (Swift and Proctor, 1977; Hahn et al., 1993). A steady flow rather than a cyclic unsteady flow was used in this case to allow the results to emphasize the airflow dynamics and patterns independent from cyclic conditions. Moreover the significance of the fluctuating sinusoidal pattern of the inhalation–exhalation breathing cycle on the nasal airflow can be estimated by examining the Womersley number, α and the Strouhal number, S. The calculated Womersley number:

$$\alpha = \frac{D}{2}\left(\frac{\omega}{\nu_g}\right)^{0.5} \tag{1}$$

was 1.68 while the Strouhal number:

$$S = \frac{\omega D}{u_{ave}} \tag{2}$$

was 0.01. D is equal to 0.01 m and is the characteristic length which was taken as the average hydraulic diameter of 30 cross-sections taken throughout the nasal cavity. ν_g is the kinematic viscosity of air and ω is the breathing frequency equal to $\omega = 2\pi f = 1.57\ s^{-1}$ and u_{ave} is the average velocity through the nasal passage under the flow rate of 15 L/min which is equal to 0.9 m/s. Although the Womersley number is greater than 1, it is not much greater, while the low value for S suggests that the flow may be assumed to be quasi-steady. It has also been shown experimentally that the oscillatory effects are not present until $\alpha \geq 4$ (Isabey and Chang, 1981). Additionally other studies have concluded that under most conditions especially low flow rates, the nasal airflow can be considered quasi-steady (Chang, 1989; Hahn et al., 1993; Sullivan and Chang, 1991).

The steady-state continuity and momentum equations for the gas phase (air) in Cartesian tensor notation are:

$$\frac{\partial}{\partial x_i}(\rho_g u_i^g) = 0 \tag{3}$$

$$\rho u_j^g \frac{\partial u_i^g}{\partial x_j} = -\frac{\partial p_g}{\partial x_i} + \frac{\partial}{\partial x_j}\left(\mu_g \frac{\partial u_i^g}{\partial x_j}\right) \tag{4}$$

where u_i^g is the ith component of the time-averaged velocity vector and ρ_g is the air density.

For the boundary conditions, a no slip flow velocity on the passage surfaces was assumed. At the nostril, a uniform flow perpendicular to the inlet was specified which is a reasonable approximation. Keyhani et al. (1995) specified the velocity profile at the nostril based on experimental data which showed that for a given flow rate the downstream flow field is not significantly affected by the details of the velocity profile at the nostril. Additionally the flow rates of left and right nostrils are assumed to be the same. This does not simulate real breathing perfectly since the flow is induced at the larynx drawing the air from the nostrils which is affected by geometrical differences leading to varied flow rates between the cavities. However, for this paper, the focus was to present the ability of CFD to capture the micro fluid structures that exist in flow patterns within the left and right cavities under a steady-state solution while being able to compare these results against available experimental data that are based on a fixed flow rate through each cavity (Keyhani et al., 1995; Subramaniam et al., 1998). Therefore, it was important to maintain similar settings and to keep the flow rates the same between the two cavities. At the outlet a straight extension was created to allow for an outflow boundary condition that was based on the Neumann condition:

$$\frac{\partial \phi}{\partial x_n} = 0 \tag{5}$$

where the derivative of the transported variable ϕ normal to the boundary face is set to zero. The transported variable, ϕ at the boundary is extrapolated along the stream-wise direction of the fluid flow within the domain at each iteration.

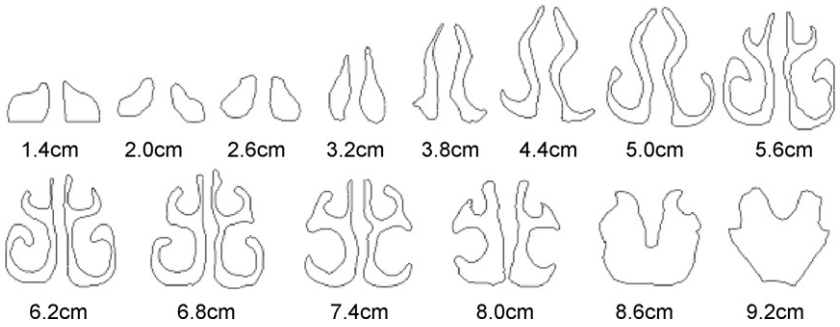

Fig. 3. 2D cross-sections of a nasal cavity of an adult male subject.

3. Results

3.1. Geometry comparisons

Fourteen cross-sections evenly spaced apart in the x-direction (Fig. 3) were created and used to calculate the averaged flow properties. The cross-sectional areas versus distance from the anterior tip of the nose of the left and right cavities were compared (Fig. 4). In the anterior region of the nasal cavity ($x < 26$ mm) and the posterior turbinate region ($x > 44$ mm), the cross-sectional area of the right cavity is larger than that of the left, while in the middle region the right side is smaller than the left.

The present computational model was compared with other nasal cavities where existing data were available (Fig. 4). Although intersubject variations in nasal cavity geometries exist, a general trend can be observed on a macro level. For example a local minimum is found for all profiles just after the inlet where the nasal valve region exists. The nasal valve is the narrowest region where the cross-sectional area was found to be 1.4 cm^2 which compares with 1.6 cm^2, 1.9 cm^2 and 2.0 cm^2 for Subramaniam et al. (1998), Cheng et al. (1996) and Keyhani et al.'s (1995) models, respectively. At the anterior turbinate region the airway expands to accommodate the olfactory sensors and the turbinate bone projections. This is reflected by an increase in the cross-sectional profiles which is observed immediately after the nasal valve region. For the current geometry, the nasal valve region is located about 2.0 cm from the anterior tip of nose, which compares with the other models that are all located around 3.0 cm away from the anterior tip of nose (Fig. 4).

3.2. Model validation

The average pressure drop between the nostril and nasopharynx was obtained at flow rates from 7.5 L/min to 40 L/min (Fig. 5). At these flow rates, the corresponding range of Reynolds numbers at the inlets is 555–2424. A laminar model for the flow rates 7.5–15 L/min and the low Reynolds k–ω turbulent model for the flow rates 20–40 L/min were used to simulate the flow field. The model equations for the turbulent model is not given in this paper for brevity as the study's focus and further results are based on a presumed laminar flow condition for flow rates of 7.5 L/min and 15 L/min only. The numerical results show good agreement with reported experimental data especially at flow rates less than 20 L/min.

3.3. Resistance and wall shear stress

Nasal resistance is an important factor in considering airway resistance. In adults, nasal resistance can contribute up to half of the total airway resistance (Bailey, 1998). As shown in Fig. 6, the

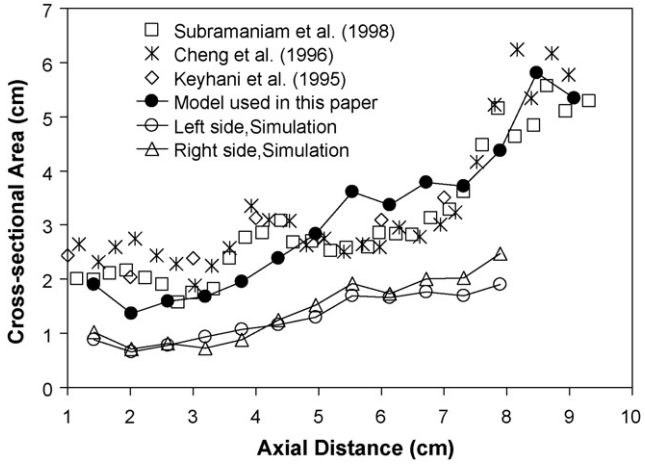

Fig. 4. The comparison of cross-sectional areas vs. distance from anterior tip of nose for different geometries: the cross-sectional area of each side for the nose used in this paper and of both sides for different geometries.

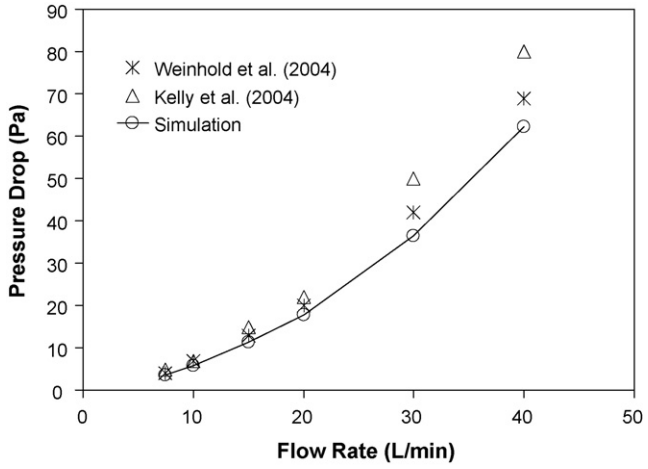

Fig. 5. Pressure drop across the human nasal cavity as a function of inspiratory flow rate compared with reported experimental data.

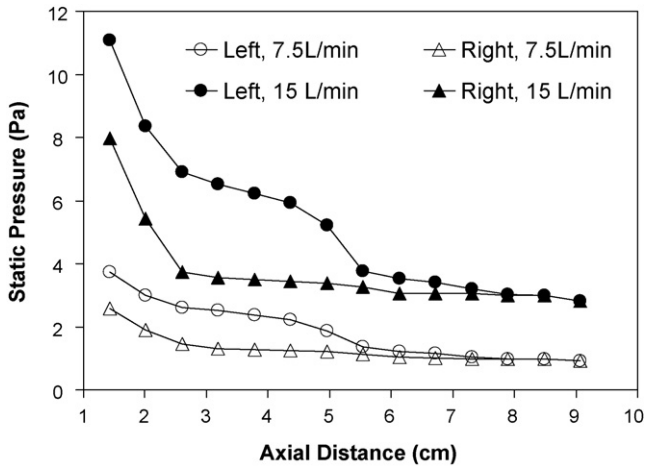

Fig. 6. Area-averaged static pressure on different coronal cross-sections vs. distance from anterior tip of nose: at flow rates of 7.5 L/min and 15 L/min.

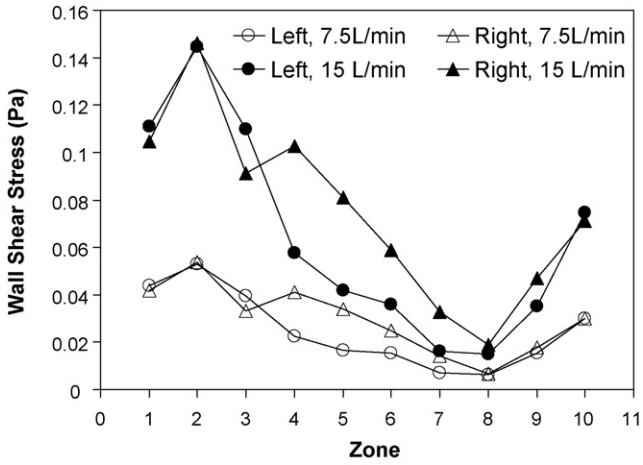

Fig. 7. Area-averaged wall shear stress on different zones surface: at flow rates of 7.5 L/min and 15 L/min.

static pressure profile decreases as the distance from the anterior nose increases. Less resistance is found for the left side where the pressure decrease is not as great as found in the right side. The influence of geometrical variations was found to produce dramatic increases in the resistance when the cross-section was reduced. In the frontal regions where x is less than 2.66 mm, the majority of the nasal resistance to airflow is produced.

3.4. Wall shear stress contours on the wall

The average wall shear stress for each subdivided zone (see Fig. 1) was calculated by summing the local shear stress at each surface and dividing by the total number of surfaces within each zone. For a Newtonian fluid, the average wall shear stress induced by the flowing air on the gas–wall interface is given by

$$\tau_{\text{ave}} = \frac{\sum_{i=1}^{x}(\mu(\partial U/\partial n))_i}{x} \quad (6)$$

where μ is the gas viscosity, x is the number of cells along a wall and n is the unit vector normal to the cavity surface. The general trend for the wall shear stress at different rates is similar (Fig. 7). The highest wall shear stresses are found in Zone 2 where the nasal valve exists. Additionally the flow in this region has changed direction from vertically aligned to a horizontal direction (Fig. 1) which causes the high stresses. The wall shear stress decreases gradually corresponding to the airway expansion in the middle region where the velocity decreases. Minimum values are found in Zone 8 before increasing again. The increase

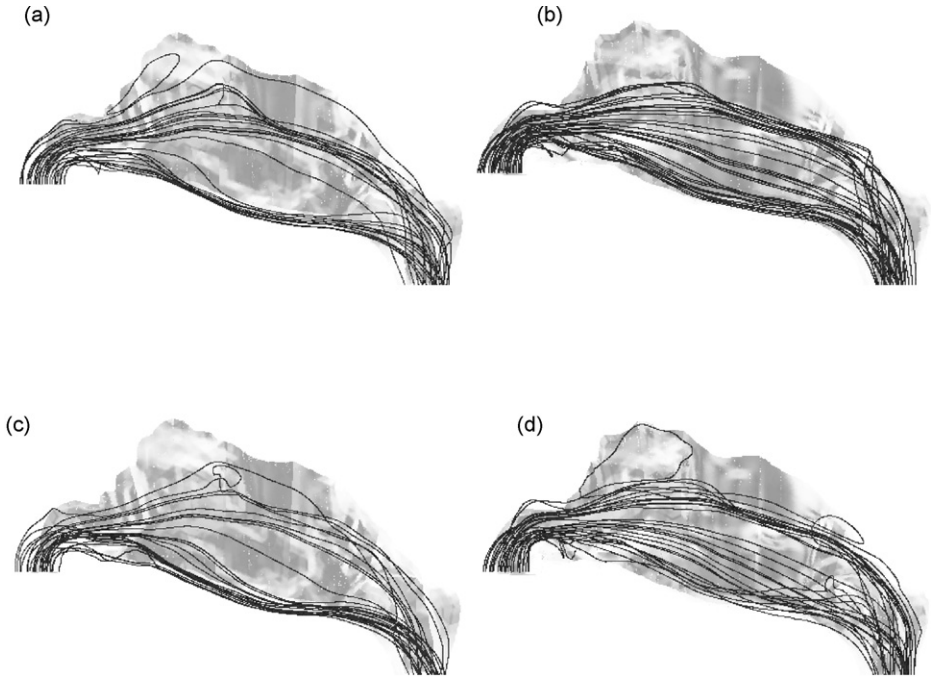

Fig. 8. Representation of flow streamlines in current nasal cavity: (a) left cavity, 7.5 L/min, (b) right cavity, 7.5 L/min, (c) left cavity, 15 L/min and (d) right cavity, 15 L/min.

is caused by the two cavities merging and a change in the flow direction at the nasopharynx where the air travels downwards towards the lungs.

3.5. Path streamlines

Path streamlines were released from the nostril inlet to provide qualitative visualisation of the flow field. The streamlines in the left nasal cavity at a flow rate of 7.5 L/min show flow separation and reversed flow just posterior to the narrowest valve (Fig. 8a). A vortex in the upper anterior part of the cavity was prominently formed. This vortex is a result of the adverse pressure gradient caused by the abrupt increase in the cross-sectional area from the nasal valve to the main nasal passage. A similar trend was found in the experimental work of Weinhold and Mlyynski (2004) and Kelly et al. (2000). As the flow rate increases to 15 L/min (Fig. 8c), the vortex moved posteriorly to the middle region of turbinate and was smaller. The streamlines in the right cavity at a flow rate of 7.5 L/min (Fig. 8b), showed no recirculation and most of the streamlines are concentrated in the middle and lower regions of the nasal cavity. At a flow rate of 15 L/min (Fig. 8d), two vortices are found. The bigger vortex is just posterior to the nasal valve while the smaller vortex is found in the posterior turbinate region. Both vortices are found in the upper region of the nasal cavity.

A comparison of streamlines produced in the literature shows similar trends (Fig. 9). Keyhani et al. (1997) found a recirculating zone downstream of the airway. The vortex extends up to the anterior end of the middle turbinate but does not reach the olfactory slit. The larger vortex is found in the upper region while a smaller vortex is found near the floor of the airway. This smaller vortex occurs directly after the nasal valve region where a favourable pressure gradient promotes flow separation. These disturbances are also found in the current simulation where the streamlines are erratic but do not reach the same magnitudes as the vortex found by Schreck et al. (1993). The simulations by Subramaniam et al. (1998) are different from all the results where prominent recirculating streams are found in the nasal vestibule and complex downward spiralling flow patterns in the nasopharynx. There is no obvious recirculation zone inside this nasal cavity.

3.6. Nasal valve flow

Two cross-sectional areas located just proximal to the anterior nasal valve at 2.6 cm and 3.2 cm were chosen to reflect the rapid changes in the flow field since the anterior nasal valve was located at 2 cm posterior to the anterior nares. The naming convention used in this paper for the left and right cavity takes on the side that the cavity sits anatomically. The cross-section shown in Fig. 10 is from a frontal perspective (positive flow into the paper) and therefore the right cavity is depicted on the left side. A contour plot of the axial velocity (x-component of velocity) is combined with streamlines of secondary flow (y–z component of velocity). The red contours suggest the main flow field, since the horizontal direction of flow is in the x-axis. By applying the directional streamlines secondary flow features such as vortices can be visualised. The air enters the vestibule region with a vertical direction. As the distance increases from the anterior tip of the nostrils, the nasal geometry becomes narrow as the airstream turns posteriorly, approximately 90° towards the nasopharynx. This transition coupled with the narrowing geometry forces the flow to emerge from

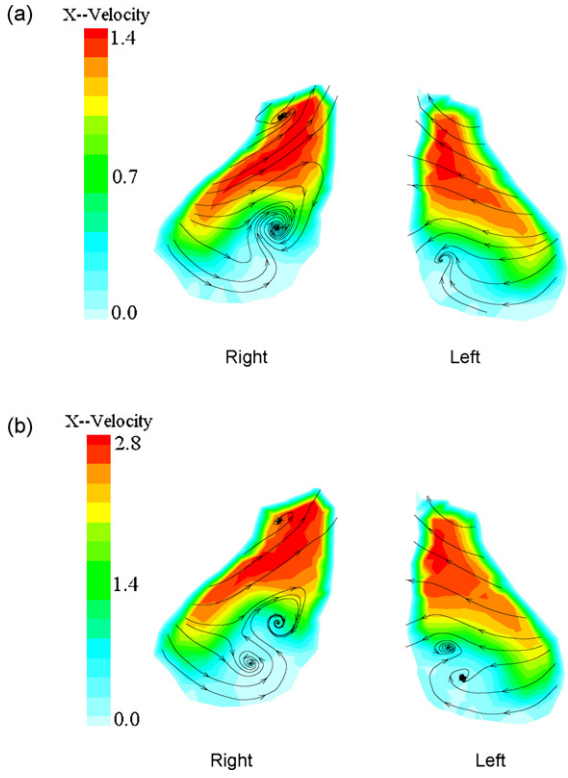

Fig. 10. Velocity field in the coronal cross-section located at 2.60 cm from the anterior tip of the nose: at flow rate of (a) 7.5 L/min and (b) 15 L/min.

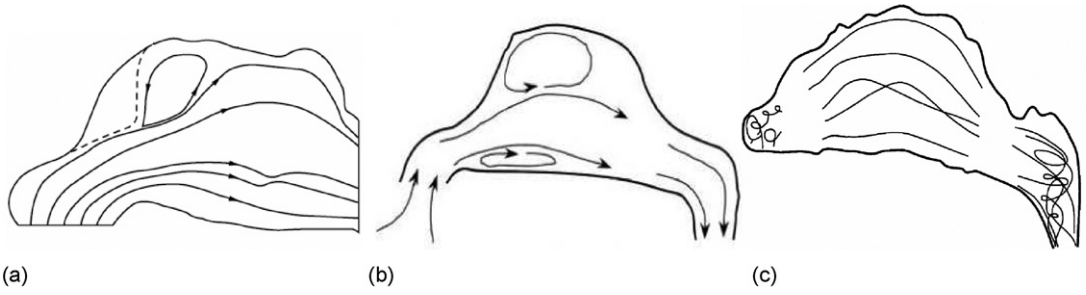

Fig. 9. Representation of flow streamlines in other nasal cavities: (a) Keyhani et al. (1997), (b) Schreck et al. (1993) and (c) Subramaniam et al. (1998).

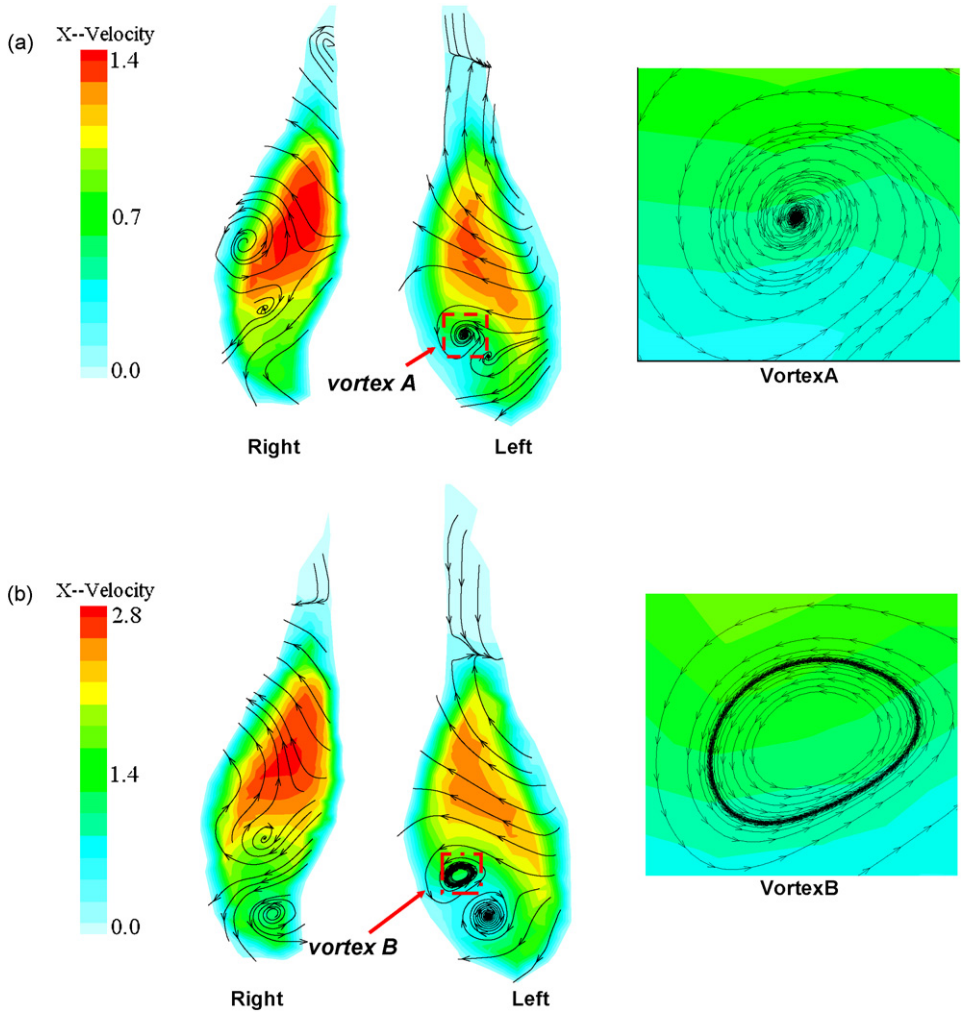

Fig. 11. Velocity field in the coronal cross-section located at 3.20 cm from the anterior tip of the nose: at flow rate of (a) 7.5 L/min and (b) 15 L/min.

the outer walls from the septum and directed inwards. The presence of the wall along with the bulk flow that exists in the upper regions restricts the flow in the lower regions (light blue colour) and forces the flow to recirculate thus formulating vortices (Figs. 10 and 11).

For the cross-section located at 2.6 cm from the anterior tip of the nose, two vortices in the right cavity and one in the left are found for a flow rate of 7.5 L/min (Fig. 10a). When the flow rate increases to 15 L/min, the number of vortices in both the cavities increases in the low flow regions and the streamlines are more dispersed (Fig. 10b). At the cross-section located at 3.2 cm from the anterior tip of the nose the bulk flow is concentrated more centrally as the airstream is developing (Fig. 11). At a flow rate of 7.5 L/min, there are two vortices in the left cavity while in the right cavity some recirculation occurs forming weaker vortices (Fig. 11a). The direction of the streamlines in vortex A all point to the centre of the vortex, which demonstrates that the axial velocity gradient is positive and the pressure gradient is negative along the axial direction (Stabl, 1992; Escudier, 1988) As the flow rate increases to 15 L/min, the magnitude of the recirculation and hence the vortices increase (Fig. 11b). The direction of all the vortices except for the upper vortex in the left cavity (vortex B) all point inwards. Vortex B shows the outer streamlines of the vortex directed inwards while the inner streamlines are directed outwards from the centre. This streamline feature is a case of a Hopf bifurcation from the mathematics branch of bifurcation theory which suggests that the positive velocity gradient changes from positive to a negative gradient (Escudier, 1988).

3.7. Middle turbinate flow

The same contour–streamline plot was applied to the middle turbinate area located at 6.10 cm from the anterior nares. The streamlines show that flow is directed downwards with the bulk flow concentrated in the upper and lower region close to the septum walls. There are no visible vortices but some weak recirculation occurs, possibly due to the narrow geometry (Fig. 12). Velocities in this region are lower than in the nasal valve region as the geometry has expanded. The downward direction is due to the airway which is now heading towards the nasopharynx. Therefore, the overall flow path undertakes a U-turn shape where the flow enters upwards, travels horizontally and end downwards towards the lungs.

To further study and compare the distribution of airflow in the turbinate region with other work in the literature, the cross-section in the middle turbinate region was subdivided into

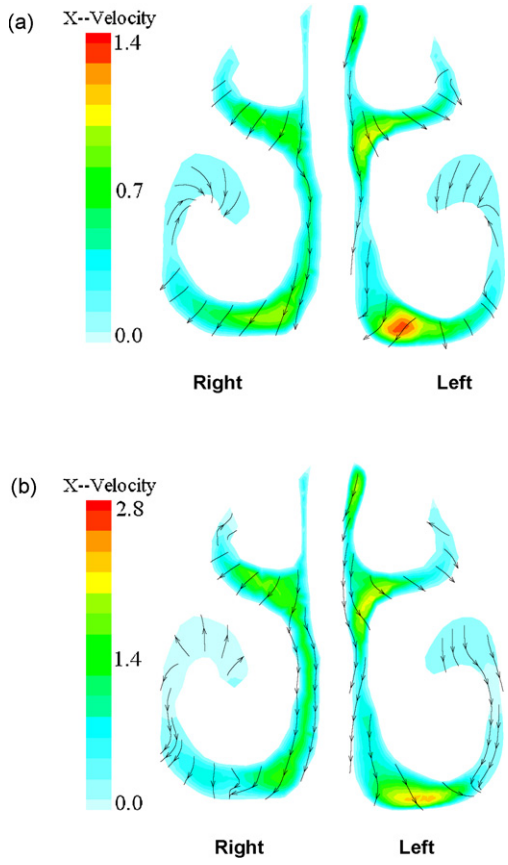

Fig. 12. Velocity field in the coronal cross-section located at 6.10 cm from the anterior tip of the nose: at flow rate of (a) 7.5 L/min and (b) 15 L/min.

separate regions and labelled from A to E. This enabled measurements of the local distribution (Fig. 13). Local volumetric flow was determined by integrating the velocity component normal to the plane over the cross-sectional area of each region. The results of the airflow distribution at a flow rate of 15 L/min for left and right sides are given in Table 1. There are obvious differences between the comparative geometries of Keyhani et al. (1995), Subramaniam et al. (1998) and the current model in this study (Fig. 13). The most striking difference is that the current model only has two meatus extensions (B′ and F′) in comparison with the other models that have three extensions: B′, C′, F′ for Keyhani et al. (1995) and B′, D′, F′ for Subramaniam et al. (1998). The cross-sections are all located at a similar region in the nasal airway—in the middle of nasal turbinate. The location of our model is located at 6.1 cm away from the anterior tip of nose while for Keyhani et al. (1995) (Fig. 13b) and Subramaniam et al. (1998) (Fig. 13c) the locations are 6.2 cm and 6.0 cm, respectively. The $\%Q_{\text{total}}$ describes the proportion of flow as a percentage of the total flow rate. The main flow direction is not easily specified for complex geometries such as that of the nose. Therefore, the average velocity magnitudes $U = (u_x^2 + u_y^2 + u_z^2)^{1/2}$ and U_x in the x-direction (axial) are used for analysis.

The flow analysis through the left cavity (Table 1) shows that 85% of the air passes through the superior medial airway (region C), the middle medial airway (region D) and the ventral medial airway (region E). These regions cover 59% of the entire cross-section. The right cavity is slightly wider and the regions C′, D′ and E′ take up 61.6% of the right section while the $\%Q_{\text{total}}$ is 94%. Despite the small difference in area coverage, region D in the left cavity exhibits a small constricting section which causes a higher resistance in the flow and hence the smaller proportion of airflow through C, D and E. For Keyhani et al. (1995) model, the majority of the flow occurs in C′ and E′ (56% in total) which are the central and lower passages. The flow also dominates in similar regions D′ and E′ for Subramaniam et al. (1998) totalling 71% (Table 2).

The flow in the left cavity stays close to the wall while its distribution is mainly in the middle sections and more dominant in the lower sections while a small percentage (11.6%) is found in the upper section. This pattern was also observed in the work by Hahn et al. (1993) and in Keyhani et al.'s (1995) model.

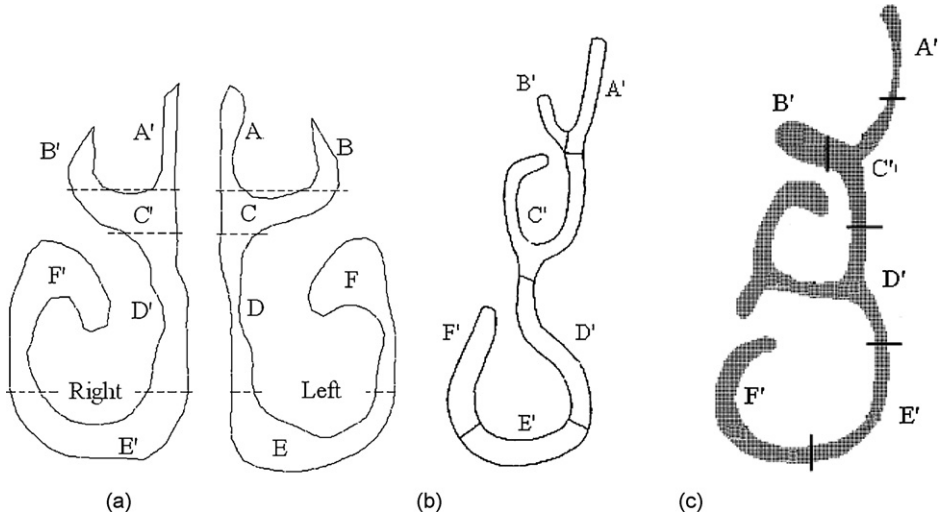

Fig. 13. The coronal sections are divided into sub-sections which are indicated by letters: the section is located at (a) 6.1 cm from the anterior tip of the nose used in this paper, (b) 6.2 cm from the anterior tip of the nose used by Keyhani et al. (1995) and (c) 6.0 cm from the anterior end of the nose used by Subramaniam et al. (1998).

Table 1
Flow distribution on the plane in the middle of turbinate for flow rate of 15 L/min

Region	Left					Right				
	A (mm^2)	Q (mL/s)	Q_{total} (%)	U (m/s)	U_x (%)	A (mm^2)	Q (mL/s)	Q_{total} (%)	U (m/s)	U_x (%)
A′	13.7	13.9	11.6	1.3	78.1	10.4	3.1	2.5	0.42	70.5
B′	9.7	1.4	1.2	0.2	62.6	8.6	1.6	1.3	0.24	75.6
C′	23.2	25.6	21.4	1.4	79.2	29.1	28.5	23.7	1.12	87.1
D′	21.6	24.4	20.3	1.2	90.8	36.9	34.7	28.8	1.00	94.2
E′	50.3	52.4	43.7	1.1	95.8	50.5	50.2	41.7	1.06	93.8
F′	42.8	2.2	1.8	0.1	80.0	53.5	2.5	2.1	0.11	41.8
Total	161.3	119.9				189.0	120.5			

Table 2
Flow distribution on the right plane in the middle of turbinate for flow rate of 15 L/min

Region	Keyhani et al. (1995)					Subramaniam et al. (1998)				
	A (mm^2)	Q (mL/s)	Q_{total} (%)	U (m/s)[a]	U_x (%)	A (mm^2)	Q (mL/s)	Q_{total} (%)	U (m/s)	U_x (%)
A′	15.6	14.1	11.4	–	0.91	7.9	2.1	1.9	0.51	52.9
B′	6.0	3.8	3.0	–	0.63	15.4	2.1	1.9	0.24	58.3
C′	35.5	34.2	27.3	–	0.96	20.8	12.9	11.3	0.78	79.5
D′	27.9	22.8	18.3	–	0.82	54.8	53.2	46.7	1.20	87.5
E′	27.9	35.9	28.7	–	1.29	20.5	27.8	24.4	1.39	97.8
F′	26.5	14.1	11.3	–	0.53	28.9	15.8	13.9	0.79	69.6
Total	139.4	124.9				148.3	113.9			

[a] Data not available.

In the right cavity the flow is concentrated within the middle sections. The flow in the left olfactory slit (section A) is found to be larger than that of the right side (zone A′). The axial flow value was represented by the x-component of velocity U_x (%) as a percentage of the total velocity magnitude U were high which implies that the flow is dominant in the x-direction. Low velocity regions found in B′ and F′ for all the models show a much lower axial velocity. These regions become susceptible to recirculating flows as they are far away from the bulk flow regions.

4. Discussion

The main distinctions of the reconstructed nasal cavity used in this paper in comparison with others are: (i) a narrower nasal valve region, (ii) wider turbinates and (iii) a shorter length. Our model exhibited the smallest cross-sectional area for the nasal valve region but had the largest cross-sectional area in the turbinate region when compared with other models. The differences in geometry for the left and right sides as well as intersubject variations, provided differences in the airflow patterns. For example an increase in the inspiratory flow rate resulted in higher wall shear stresses as well as magnifying the local differences between the left and right cavities, where they exist (e.g. Zones 4–6). As shear stresses are linearly related to the local velocity, these values significantly increase as breathing efforts increase. High shear stresses that are concentrated locally may cause irritation of the blood vessels within that area. Maximum shear stresses found by Elad et al. (1993) were in the range of 0.2 Pa on the septal wall across the inferior turbinate at near peak inspiration of 20 L/min, while Nucci et al.'s (2003) values were in the range of 1.5–2 Pa in uniform regions of large arteries. The maximum shear stresses that occurred in the nasal valve region and to a lesser extent in Zone 3 and 4, may lead to dysfunctional effects on nasal sensation of airflow and may play a role in the well-being of nasal breathing. By mapping out the distribution of external stresses on the nasal cavity walls, predictions of the mechanoreceptor response may be estimated.

Path streamlines were investigated and compared. This provided a pictorial view of macro flow features in terms of the recirculation zones that is important in the study of gas–particle flows within the airway. It was found that recirculation was prevalent in the olfactory region and in the nasal valve region where the flow experiences sharp changes in the flow conditions. There were some differences in the size and location of the vortices between the models compared which may be attributed to geometrical differences such as an increase in airway height that was found to promote separation by Keyhani et al. (1997).

The internal nasal valve is considered as a region rather than an oblique cross-sectional area of the nasal passageway and resembles a constriction–expansion region which causes the majority of the total airflow resistance. The streamlines in the anterior nasal valve are all directed from the outer wall towards the inner septum wall (Fig. 10). In the right cavity however, the opposite occurs (Fig. 11). The flow is directed from the inner side, outwards. Further examination of the streamlines in cross-sections further downstream reveal that the secondary flow direction in the left cavity indeed changes similar to the right cavity. Therefore, the authors believe that the flow development in the right cavity is quicker than the left. As the air enters the nasal valve region after the 90° turn, the transition coupled with the narrowing geometry forces a majority of the flow direction to come from the opposite side

of the septum walls. This is consistent with the larger contour areas (red colour) of high velocity found for the right cavity. After the flow is aligned and the airway begins to expand the resistance at the walls causes the flow to rebound and flow in the opposite direction. For particle deposition studies this flow feature is important as it allows better prediction of deposition sites. The direction of the streamlines that initially accelerate from the outer wall will enhance the deposition of inhaled particles onto the inner nasal septum wall side rather than on the outer surfaces. The complex flow in the nasal valve region therefore acts as a filtration device for particle deposition—a fact that is positive for toxic inhalation but a problem for drug delivery.

The turbinate region consists of a narrow curled bone that protrudes into the main airway. The middle and inferior turbinate is an important structure for filtration, heating and humidification where the mucosal wall surface area is increased. Intersubject geometric variations is thought to arise from eco-geographic adaptation to climate where nasal cavities have been broadly categorised as leptorrhines (tall and narrow) or platyrrhines (short and broad) according to their morphology. It is thought that people exposed to cold dry environments exhibit leptorrhine features that induce turbulent flow features (Wolpoff, 1968; Weiner, 1954). While those exposed to hot humid environments exhibit platyrrhine features that produce more laminar flow, where the conditioning of the air is less critical (Churchill et al., 2004; Carey and Steegmann, 1981). This suggests that the efficiency of the turbinates to heat and humidify the air due to the increase in surface area of the meatus regions is very low. Since only a small percentage of air reaches this outer meatus region (F) the heating and humidifying ability of the turbinates affects less than 2% of the flow field. Therefore, the role of the turbinates to condition the air may not be solely reliant on the surface area contact but may in fact be influenced by the nature of the flow that the turbinates cause. For example, the protrusions create narrow meatus airways which affect the flow regime (laminar or turbulent) and hence the heating capability. Further studies into this effect are therefore needed. Finally the high flow rates found in region A and A′ may be considered as undesirable since it can lead to damage to the olfactory regions. Normally low flow characteristics are required in the olfactory region as it is a defense mechanism that prevents particles whose trajectories are heavily dependent on flow patterns from being deposited onto the sensitive olfactory nerve fibers, while vapors are allowed to diffuse for olfaction.

5. Conclusion

To better understand the physiology of the nose, the airflow patterns and distribution was investigated and compared with available data. The computational model based on CT scans of an Asian male volunteer exhibited a narrower nasal valve region, wider turbinates and a shorter length in comparison with other models. Despite this a general trend was observed for the cross-sectional area profile of the airway along the axial distance. Nasal resistance was found to contribute up to half of the total airway resistance within the first 2–3 cm of the airway. The formation of vortices was found primarily in the upper olfactory region and just posterior to the nasal valve where the geometry begins to expand. Further investigation into the nasal valve region found multiple local secondary flow regions that existed in the lower regions away from the bulk flow that travelled within the middle regions. The majority of the flow in this region remained close to the septum walls and only a small proportion reached the olfactory region and the outer meatus extensions that were created by the turbinate protrusions. Low flow in the olfactory region is a defense mechanism that prevents particles whose trajectories are heavily dependent on flow patterns from being deposited onto the sensitive olfactory nerve fibers, while vapors are allowed to diffuse for olfaction. However, the low flows in the meatus regions brings into the question the efficiency of the turbinate protrusions condition the inspired air.

References

Bailey, B. (Ed.), 1998. Head and Neck Surgery: Otolaryngology, 2nd ed. Lippincott-Raven, New York, NY, pp. 335–344, 376, 380–390.

Carey, J.W., Steegmann, A.T.J., 1981. Human nasal protrusion, latitude, and climate. Am. J. Phys. Anthropol. 56, 313–319.

Chang, H.K., 1989. Flow dynamics in the respiratory tract. In: Chang, H.K., Paiva, M. (Eds.), Respiratory Physiology, An Analytical Approach. Dekker, New York.

Cheng, Y.S., Yeh, H.C., Guilmette, R.A., 1996. Nasal deposition of ultrafine particles in human volunteers and its relationship to airway geometry. Aerosol Sci. Technol. 25, 274–291.

Churchill, S.E., Shackelford, L.L., Georgi, J.N., Black, M.T., 2004. Morphological variation and airflow dynamics in the human nose. Am. J. Hum. Biol. 16, 625–638.

Elad, D., Liebenthal, R., Wenig, B.L., Einav, S., 1993. Analysis of air flow patterns in the human nose. Med. Biol. Eng. Comput. 31, 585–592.

Escudier, M., 1988. Vortex breakdown: observations and explanations. Prog. Aerospace Sci. 25, 189–229.

Hahn, I., Scherer, P.W., Mozell, M.M., 1993. Velocity profiles measured for airflow through a large-scale model of the human nasal cavity. J. Appl. Physiol. 75 (5), 2273–2287.

Isabey, D., Chang, H.K., 1981. Steady and unsteady pressure–flow relationships in central airways. J. Appl. Physiol. 51, 1338–1348.

Kelly, J.T., Prasad, A.k., Wexler, A.S., 2000. Detailed flow patterns in the nasal cavity. J. Appl. Physiol. 89, 323–337.

Keyhani, K., Scherer, P.W, Mozell, M.M., 1995. Numerical simulation of airflow in the human nasal cavity. J. Biomech. Eng. 117, 429–441.

Keyhani, K., Scherer, P.W., Mozell, M.M., 1997. A numerical model of nasal odorant transport for the analysis of human olfaction. J. Theor. Biol. 186, 279–301.

Nucci, G., Suki, B., Lutchen, K., 2003. Modeling airflow-related shear stress during heterogeneous constriction and mechanical ventilation. J. Appl. Physiol. 95, 348–356.

Robert, G.H., 2001. Forced inspiratory nasal flow–volume curves: a simple test of nasal airflow. Mayo Clin. Proc. 76, 990–994.

Schreck, S., Sullivan, K.J., Ho, C.M., Chang, H.K., 1993. Correlations between flow resistance and geometry in a model of the human nose. J. Appl. Physiol. 75 (4), 1767–1775.

Stabl, W.H., 1992. Experimental investigation of the vortex flow on delta wings at high incidence. AIAA J. 30 (4), 1027–1032.

Subramaniam, R.P., Richardson, R.B., Morgan, K.T., Kimbell, J.S., Guilmette, R.A., 1998. Computational fluid dynamics simulations of inspiratory airflow in the human nose and nasopharynx. Inhal. Toxicol. 10, 91–120.

Sullivan, K.J., Chang, H.K., 1991. Steady and oscillatory trans-nasal pressure–flow relationships in healthy adults. J. Appl. Physiol. 71, 983–992.

Swift, D.L., Proctor, D.F., 1977. Access of air to the respiratory tract. In: Brain, J.D., Proctor, D.F., Reid, L.M. (Eds.), Respiratory Defence Mechanisms. Part 1. Marcel Dekker, New York, NY, pp. 63–93.

Wang, K., Denney Jr., K., Morrison, E.E., Vodyanoy, V.J., 2005. Numerical simulation of air flow in the human nasal cavity. In: Proceedings of the 2005 IEEE, pp. 5607–5610.

Weiner, J.S., 1954. Nose shape and climate. Am. J. Phys. Anthropol. 12, 615–618.

Weinhold, I., Mlyynski, G., 2004. Numerical simulation of airflow in the human nose. Eur. Arch. Otorhinolaryngol. 261, 452–455.

Wolpoff, M.H., 1968. Climatic influence on the skeletal nasal aperture. Am. J. Phys. Anthropol. 29, 405–424.

Zamankhan, P., Ahmadi, Wang, Z.C., 2006. Airflow and deposition of nanoparticles in a human nasal cavity. Aerosol Sci. Technol. 40, 463–476.